Quantification and Tuning of Surface Oxygen Vacancies for the Hydrogenation of CO_2 on Indium Oxide Catalysts

Robert Baumgarten[1], Raoul Naumann d'Alnoncourt[1,*], Stephen Lohr[1,2], Esteban Gioria[1], Elias Frei[2], Edvin Fako[2], Sandip De[2], Chiara Boscagli[3], Matthias Drieß[1,4], Stephan Schunk[2,3,5], and Frank Rosowski[1,2]

DOI: 10.1002/cite.202200085

Supporting Information available online

The direct hydrogenation of CO_2 to methanol is an attractive approach to employ the greenhouse gas as a chemical feedstock. However, the commercial copper catalyst, used for methanol synthesis from CO-rich syngas, suffers from deactivation at elevated CO_2 partial pressure. An emerging alternative is represented by In_2O_3 as it withstands the hydrothermal conditions induced by the reverse water-gas shift reaction. The active sites for the adsorption of CO_2 and the subsequent conversion into methanol were shown to be oxygen vacancies on the surface of In_2O_3. In this study, N_2O was utilized as a probe molecule to quantify the number of vacancies on indium oxide catalysts. The number of inserted oxygen atoms could be correlated to the respective CO_2 hydrogenation activity. Furthermore, the atomic efficiency of indium was enhanced by applying atomic layer deposition of indium oxide on ZrO_2.

Keywords: CO_2, Hydrogenation, Indium oxide, Methanol, N_2O reactive frontal chromatography

Received: June 01, 2022; *revised:* August 12, 2022; *accepted:* September 01, 2022

1 Introduction

The efficient utilization of CO_2 as feedstock for the chemical industry would be a highly appreciated instrument to mitigate carbon emissions [1]. CO_2 generated as by-product along the chemical value chain could be re-introduced by subsequent valorization processes to facilitate a circular economy. For instance, CO_2 can be converted into syngas (CO, H_2) by dry reforming of methane or reduced to more reactive CO via the reverse water-gas shift reaction (RWGS, Eq. (1)) [2, 3]. The direct hydrogenation to hydrocarbons or methanol is of particular interest due to the rising strive for a hydrogen-based industry. Ideally, the CO_2 is captured from the earth atmosphere and combined with green hydrogen from sustainable sources, so that the methanol itself becomes sustainable [1, 4].

$$\begin{aligned} &CO_{2(g)} + H_{2(g)} \rightleftharpoons CO_{(g)} + H_2O_{(g)} \\ &\Delta G^0_{298.15K} = +28.6\ \text{kJ mol}^{-1} \end{aligned} \tag{1}$$

Methanol is among the most produced compounds with a yearly production of about 105 Mt in 2021 [5]. It is mainly used as intermediate for the fabrication of formaldehyde or methyl tert-butyl ether (MTBE) and is a potential liquid energy carrier of the future. Thereby, it can be employed in methanol fuel cells to generate electricity or as a propellant for combustion engines [6, 7].

[1]Robert Baumgarten, Dr. Raoul Naumann d'Alnoncourt, Stephen Lohr, Esteban Gioria, Prof. Dr. Matthias Drieß, Dr. Stephan Schunk, Dr. Frank Rosowski
r.naumann@bascat.tu-berlin.de
BasCat – UniCat BASF JointLab, Technische Universität Berlin, 10623 Berlin, Germany.

[2]Stephen Lohr, Dr. Elias Frei, Dr. Edvin Fako, Dr. Sandip De, Dr. Stephan Schunk, Dr. Frank Rosowski
BASF SE, Carl-Bosch-Straße 38, 67056 Ludwigshafen, Germany.

[3]Dr. Chiara Boscagli, Dr. Stephan Schunk
hte GmbH, Kurpfalzring 104, 69123 Heidelberg, Germany.

[4]Prof. Dr. Matthias Drieß
Technische Universität Berlin, Institut für Chemie: Metallorganik und Anorganische Materialien, Straße des 17. Juni 135, 10623 Berlin, Germany.

[5]Dr. Stephan Schunk
Universität Leipzig, Institut für Technische Chemie, Linnéstraße 3, 04103 Leipzig, Germany.

Nowadays, methanol is conventionally synthesized from CO-rich syngas (CO, CO_2, H_2) over a copper-zinc catalyst at 50–100 bar and 200–300 °C [8]. Typically, the CO_2 content is minimized as the selectivity for the reverse water-gas shift reaction (RWGS (Eq. (1)) intensifies with a rising partial pressure of CO_2 [9, 10]. Additionally, the direct hydrogenation of CO_2 to methanol generates water as by-product (Eq. (2)) and is less exothermic than the direct hydrogenation from CO (Eq. (3)) [11]. The resulting water leads to hydrothermal conditions causing severe changes of the Cu/ZnO interface and reduction of the hydrogenation activity [12–14]. Therefore, the partial pressure of CO_2 is kept low to ensure long-term stability of copper-zinc based catalysts.

$$\begin{aligned} &CO_{2(g)} + 3H_{2(g)} \rightleftharpoons CH_3OH_{(g)} + H_2O_{(g)} \\ &\Delta G^0_{298.15K} = +3.5\ \text{kJ mol}^{-1} \end{aligned} \tag{2}$$

$$\begin{aligned} &CO_{(g)} + 2H_{2(g)} \rightleftharpoons CH_3OH_{(g)} \\ &\Delta G^0_{298.15K} = -25.2\ \text{kJ mol}^{-1} \end{aligned} \tag{3}$$

Nevertheless, for effective reduction of CO_2 emissions, the CO_2 fraction of the utilized syngas should be maximized. In recent years, indium-based catalysts emerged as alternative system for the direct hydrogenation of CO_2 to methanol [15, 16]. Particularly, ZrO_2-supported In_2O_3 was shown to possess long-term stability and high hydrogenation activity under CO_2-rich conditions [17]. Furthermore, indium oxides selectivity towards methanol could be increased by adjusting the gas-hourly space velocity (*GHSV*) as the RWGS exhibits a lower reaction rate. For In_2O_3, a selectivity of nearly 100 % was reached at *GHSV* above 16 000 h^{-1} [17, 18]. Yet, the drawback of elevated flow velocities is a decreased single pass conversion of the reactant feed. On In_2O_3, the inhibition of the RWGS reaction was also predicted by density functional theory (DFT) calculations [19] and confirmed by a higher apparent activation energy for the RWGS in steady-state experiments at 50 bar [20].

As indium oxide is the main component of the catalyst system the major concern is to increase its dispersion and to maximize the accessibility of indium sites by the deposition on a carrier material [21]. Monoclinic ZrO_2 (m-ZrO_2) was found to be the most beneficial support material reaching more than ten times higher space-time yield (*STY*) compared to TiO_2, ZnO, SiO_2 or Al_2O_3 (ca. 0.33 $g_{MeOH} g_{cat}^{-1} h^{-1}$ at 300 °C) [17]. Compared to bulk In_2O_3, the indium-base *STY* was also about ten times higher when supported on ZrO_2 (ca. 0.25 vs. 3.5 $g_{MeOH} g_{Indium}^{-1} h^{-1}$). Additionally, a co-precipitation method, yielding mixed In-Zr oxides, was demonstrated to increase the indium-based CO_2 conversion rate to olefins [22–24]. However, mixed oxides were shown to have inferior performance for the hydrogenation to methanol than In_2O_3 supported on ZrO_2 [21]. The superior activity of the oxidic In-Zr interface was attributed to the favored generation of oxygen defects due to the lattice mismatch between In_2O_3 and m-ZrO_2 [21].

The consent of most studies is that oxygen deficient sites are most active for the CO_2 hydrogenation on In_2O_3 [15, 25–27]. Under reaction conditions, the surface of In_2O_3 is partially reduced by hydrogen forming under-coordinated indium sites (In_2O_{3-x}) [28]. The resulting oxygen vacancies (O_{vac}) attract the insertion of CO_2, which subsequently undergoes stepwise hydrogenation to methanol. Also hydroxylated In-sites were demonstrated to be active for CO_2 adsorption by DFT and ab initio thermodynamic studies [29]. Yet, in order to optimize the performance of indium-based catalysts, not only the nature but also the quantity of active sites should be investigated.

A prominent strategy to improve the catalytic performance is to multiply the number of surface vacancies by enhancing the dispersion of In_2O_3 [15]. Moreover, the formation of O_{vac} can be facilitated by improved H_2 activation, which was accomplished by the promotion with noble metals [30]. For example, Pd and Pt nanoparticles were shown to enhance the ability for H_2 dissociation, which aids the formation of oxygen vacancies by hydrogen spillover [31, 32]. Nevertheless, an excessive oxygen deficiency inhibits the dissociation of H_2 and hinders the subsequent hydrogenation of adsorped CO_2* [33]. Therefore, the conversion of CO_2 to methanol requires a balanced supply of both O_{vac} and surface oxygen [27].

The correlation between a materials characteristic and its CO_2 hydrogenation performance was investigated via several approaches. For example, the determination of the H_2-reducibility (via TPR), the number of heat-induced oxygen vacancies (via CO_2-TPD) and CO_2-FTIR was applied [21, 22, 32]. Yet, a follow-up study demonstrated that the H_2-reducibility and the number of heat-induced O_{vac} may not be directly related to the CO_2 conversion rate [23]. Furthermore, in an infrared spectrum the adsorption of CO_2 results in a broad range of different species and excitation modes that are difficult to quantify.

Moreover, the X-ray photoemission spectrum (XPS) of the O1s region (oxygen 1s orbital) was used to determine oxygen vacancies [22, 23, 32, 34, 35]. However, other studies demonstrated that the XPS peaks, which are often assigned to O_{vac}, rather correlate to adsorbed water or surface OH-groups (at 531–533 eV) [36, 37]. Nevertheless, electron paramagnetic resonance (EPR) was employed to verify the existence of the oxygen vacancies on the surface [17, 35, 38]. Therefore, some publications assigned the XPS signal to oxygen that is in close proximity to an oxygen defect (ca. 530.5 eV) [37, 39]. Despite the possibly correct assignment, XPS would only deliver relative O_{vac} concentrations. Consequently, there is a need for a practical quantification method of accessible oxygen vacancies on the In_2O_3 surface.

N_2O reactive frontal chromatography (RFC) is often used to determine the specific surface area of exposed copper metal on a catalyst. It was also shown that N_2O is able to

titrate oxygen vacancies on the interface between Au particles and ZnO support [40]. In this study we demonstrate the usage of N_2O RFC for the titration of oxygen vacancies at under-coordinated indium sites (O_{vac}). The method and theory are described in detail in the materials and methods section (Sect. 2.4). N_2O RFC was adapted as fingerprint method to determine the accessibility and abundance of the vacancies. Afterwards, the resulting values were correlated to the CO_2 hydrogenation activity. Moreover, atomic layer deposition (ALD) was utilized as synthesis tool to support highly dispersed indium oxide (InO_x) on ZrO_2 (Sect. 2.2). Samples prepared by ALD were compared to bulk In_2O_3 and samples deriving from incipient wetness impregnation.

2 Materials and Methods

2.1 Catalyst Synthesis

Used materials are listed in the Supporting Information (SI). Three types of indium-based catalysts were prepared and tested. Bulk In_2O_3, In_2O_3 supported on ZrO_2 via incipient wetness impregnation (IWI) and InO_x supported on ZrO_2 via atomic layer deposition (Sect. 2.2). Bulk In_2O_3 was synthesized by the calcination of precipitated $In(OH)_3$. Indium nitrate hydrate was dissolved in a solution of HPCL-grade water and ethanol with a volume ratio of 1.2 to 1. Subsequently, an aqueous solution of 90 mmol L^{-1} ammonium carbonate was added to the precursor solution with a volume ratio of 1 to 2. The resulting slurry was collected by filtration and washed with deionized water yielding $In(OH)_3$ as a solid. The precursor was dried in air at 80 °C for 12 h and calcined at 300 °C (3 K min^{-1}) for 3 h, under 20 % O_2 (in N_2) yielding bulk In_2O_3. Supported In_2O_3 was synthesized by incipient wetness impregnation (IWI) on monoclinic ZrO_2. Indium nitrate hydrate was added to HPLC-grade water that equaled the maximum water absorption of the ZrO_2 powder. The solution was distributed onto the ZrO_2 support and dried in air at 80 °C for 12 h. Subsequently, the precursor was calcined at 300 °C (3 K min^{-1}) for 3 h, under 20 % O_2 (in N_2), yielding In_2O_3/ZrO_2.

2.2 Atomic Layer Deposition of InO_x on ZrO_2

Atomic layer deposition was used to prepare highly dispersed indium oxide (InO_x) on ZrO_2, which was tested as CO_2 hydrogenation catalyst. ALD is a well-established tool for the deposition of uniform, sub-nanoscale films on different carrier materials. The technique follows sequential reactions (cycle) in which a gaseous precursor reacts with specific surface groups of a material (e.g., OH). Subsequently, excess precursor is purged out and the surface group termination is restored by dosing a reactant (e.g., water). The most commonly studied material grown by ALD is Al_2O_3, using trimethylaluminum (TMA) and water as a precursor-reactant combination [41]. ALD was shown to be applicable to materials with different topographies, such as silicon wafers [42], electrodes [43] and even polymers [44]. Therefore, it also gained recognition in the synthesis of heterogeneous catalysts [45, 46].

So far, ALD was investigated for the precise deposition of active metals [47, 48] and metal oxides [49–51]. For example, a porous alumina layer deposited by ALD on a Ni/SiO_2 catalyst prevented unwanted carbon formation under dry reforming conditions [52]. Furthermore, ALD was used to generate ZnO interfaces that facilitated the formation of Pt_1Zn_1 nano-alloys which were active for the dehydrogenation of propane (PDH) [53]. In one example for the application of indium oxide ALD, an In_2O_3 layer was grown over Pt/Al_2O_3 also resulting in an efficient PDH catalyst [50]. However, to our knowledge, there is only one example that applied ALD for the synthesis of CO_2 hydrogenation catalysts. Wang et al. [54] deposited uniform ZnO overcoats on Cu/SiO_2 which exhibited higher methanol selectivity compared to impregnated samples.

In this study, ALD experiments were carried out in a self-designed setup of which a detailed description is given elsewhere [55]. Trimethylindium (TMI) and water were used as precursor-reactant combination and the overall ALD process investigation is described in detail in [56]. Initially, the ALD growth behavior was validated by in situ thermogravimetric studies in a magnetic suspension balance (SI Fig. S1). The regarding mass uptake of InO_x on ZrO_2 during ALD is discussed in the SI.

For the catalyst synthesis, monoclinic ZrO_2 powder was filled into a tubular fixed bed reactor made of quartz glass (20 mL). The ALD process was conducted under a constant total gas flow of 100 mL min^{-1} at atmospheric pressure. The powder substrate was kept at 150 °C, the TMI dosing unit was heated to 80 °C and the water unit was kept at room temperature. Both reactants were sequentially fed into the reactor using argon as carrier and purge gas. The used ALD sequence (cycle) was TMI/Ar-purge/H_2O/Ar-purge. The point of precursor or reactant saturation was determined by online mass spectrometry. Both reactants were dosed into the reactor until the mass traces for m/z = 115 (TMI) or m/z = 18 (H_2O) reached constant levels.

2.3 Characterization of the Catalysts

Powder X-ray diffraction (XRD), inductively coupled plasma optical emission spectroscopy (ICP-OES), nitrogen physisorption measurements, temperature programmed reduction with hydrogen (H_2-TPR), X-ray photoelectron spectroscopy (XPS, under inert conditions after reduction) and scanning transmission electron microscopy (STEM) were used to analyze the samples. Detailed descriptions of the methods are provided in the Supporting Information (Sect. S2).

2.4 N_2O Reactive Frontal Chromatography as a Fingerprint Method

Usually, N_2O reactive frontal chromatography (N_2O RFC) is used to determine the specific surface area of copper metal [57, 58]. Thereby, N_2O is employed as probe molecule for the titration of reduced copper sites. In contact with copper, it decomposes into gaseous nitrogen and oxygen, which exclusively oxidizes the copper surface atoms (at RT). The number of reacted oxygens is determined by the amount of nitrogen leaving the system. Furthermore, the stoichiometry of exposed Cu and reacted oxygen is assumed to be 2:1. Finally, the surface area of exposed Cu can be calculated estimating $1.46 \cdot 10^{19}$ Cu atoms per m^2 [58]. Besides copper, also the surface area of nickel was evaluated with a similar N_2O RFC method [59].

In this study, the same principle was adapted for the investigation of oxygen deficient sites on the surface of indium-based catalysts. Under hydrogenation conditions, indium oxide holds a specific amount of indium atoms being undercoordinated by oxygen (In_2O_{3-x}). The oxygen vacancies (O_{vac}) are active sites for the insertion (chemisorption) of CO_2 [25]. After the hydrogenation to methanol, the former vacancy remains filled by an oxygen atom. Subsequently, the O_{vac} can be recreated by the heterolytic dissociation of hydrogen on the surface [28]. The dissociation forms an indium hydride (In-H) and an adjacent hydroxyl group (In-OH). Subsequently, H_2O can be released to restore the vacancy via hydride transfer from In-H to the OH group. Here, N_2O was used to imitate the oxygen insertion into the vacancies after reduction by hydrogen (Fig. 1a). Utilization of N_2O as probe molecule is more practical than adsorption of CO_2 as it can be done at standard temperature and pressure. Furthermore, the number of adsorption sites correlates directly with the amount of evolved N_2 while the adsorption of CO_2 is far more complex.

N_2O RFC was performed in a Belcat II (Microtrac MRB, Haan, Germany) at atmospheric pressure and RT (25 °C). The RFC reaction temperature is crucial when determining the specific surface area of a metal. For copper, the optimal temperature was reported to be around 300 K [57, 58]. At elevated temperatures oxidation of the subsurface intensifies while at lower temperatures, the N_2O might not be consumed quantitatively. In the case of nickel, the RFC temperature window was found to be 323 to 373 K [59]. In this study, however, N_2O RFC was applied to measure the abundance of oxygen vacancies on indium oxide under reductive conditions. At RT the reduced In_2O_3 samples were already active for quantitative decomposition of N_2O. To prevent sublayer oxidation, the temperature was not further increase. The effect of the RFC reaction temperature might be subject of future investigations.

In a typical experiment, 300 mg of an indium oxide sample is loaded as fixed bed into a glass tube with an inner diameter of 8 mm. The powder is hold in position by glasswool and the tube is assembled in an air-tight chamber with one in- and outlet. The respective gas feed passes the sample from top to bottom and the whole chamber is positioned in a tube furnace. Exhaust gas leaving the chamber is analyzed by an online mass spectrometer (MS). First, the chamber is purged by pure He (99.999 %) for 10 min (Fig. 1b). Subsequently, the chamber is heated to 275 °C (rate: 7 K min^{-1}) while dosing 30 mL min^{-1} 10 vol % H_2 (in He). The sample is reduced under 10 vol % H_2 (in He) at 275 °C for 1 h. Afterwards, the chamber is cooled down to RT (25 °C) while dosing pure He (50 mL min^{-1}). At RT, 30 mL min^{-1} 0.6 vol % N_2O (in He) is dosed until the signal (ion current) of unreacted N_2O breaks through and reaches its plateau in the MS. The amount of N_2O consumed was calculated from the time until the N_2 signal descended to its half-maximum height and the flowrate ($\dot{V}_{N2O}$) (Eq. (4) and Fig. 1c).

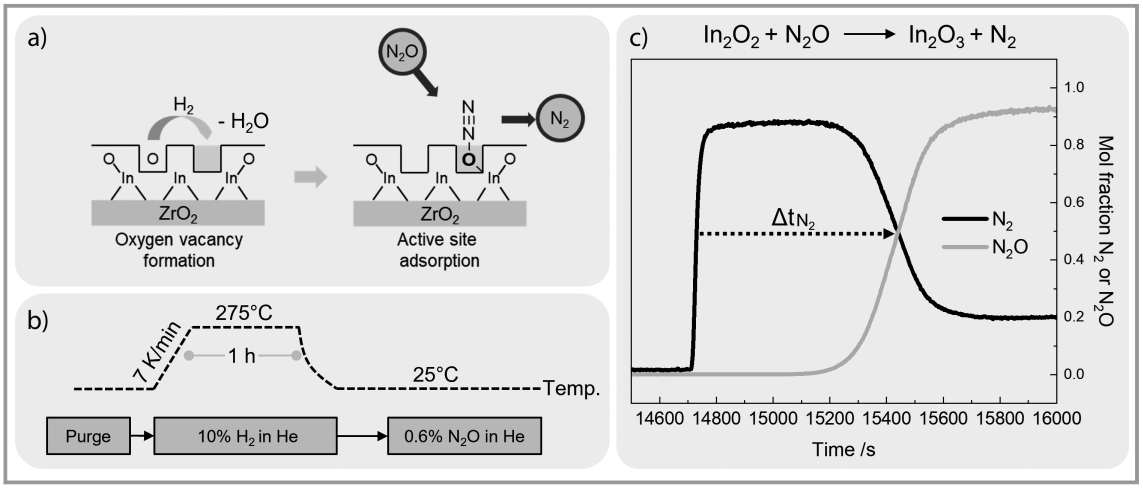

Figure 1. a) Schematic adsorption mechanism of N_2O onto supported In_2O_3. b) Experimental process of the N_2O RFC on indium oxides. c) Normalized (0,1) mol fraction of N_2 and N_2O determined by the online MS spectrometer during N_2O RFC of ALD (1c) InO_x/ZrO_2.

$$O_{(inserted)} = N_2O_{(consumed)} = \dot{V}_{N2O\ (in)}\ \Delta t_{N2\ (out)}\ \frac{p}{RT} \quad (4)$$

T and p are the standard temperature and pressure (298 K and 1 atm) and R is the gas constant. Generally, the N_2 signal reaches a maximum within seconds with every N_2O converted into N_2. After a certain time, the N_2 signal descends to its minimum and the N_2O signal rises to its global maximum. Note that a N_2 signal is further detected as it is part of the N_2O fractionation pattern. Moreover, N_2O is only converted if H_2 was dosed beforehand and the RFC process is fully reversible. Hereby, hydrogen was able to recreate the adsorption sites for N_2O, similar to the reported N_2O RFC using CO as reduction agent [60].

2.5 Catalytic Testing

Catalytic activity measurements were performed in a 16-fold parallel testing unit. Each stainless-steel reactor was loaded with 0.5 mL of a catalyst powder with a particle size of 250–315 µm. The reactors exhibited an inner diameter of 4.5 mm and the catalyst was placed as fixed bed between two layers of inert corundum. The temperature was set by a programmable furnace and monitored by thermocouples at the catalyst bed. Mass flow controllers were used to adjust the flow rates of the inlet gases Ar (99.999 %), CO (99.997 %), CO_2 (99.999 %) and H_2 (99.999 %). The effluent gas concentrations were analyzed by online gas chromatographs (GC, Agilent 7890B) equipped with two thermal conductivity detectors (TCD) and one flame ionization detector (FID) employing He as carrier gas. For each experiment, one reactor was filled exclusively with inert corundum as a reference ("ref").

Prior to the testing, the catalysts were activated in situ at 50 bar and 300 °C, in pure Ar, with a flow of 100 mL min^{-1} for 1 h. Subsequently, the temperature was reduced to 225 °C and the syngas feedstock was changed to a mixture of CO_2, CO, H_2 and Ar (17.1 vol % CO_2, 1.9 vol % CO, 76 vol % H_2 and 5 vol % Ar). The total pressure was 80 bar and the respective ratios were 9:1 for CO_2/CO and ca. 4:1 for H_2/CO_2. The volume flow was adjusted to maintain a *GHSV* of 6000 or 12 000 h^{-1}. The temperature was ramped from 225 °C to 300 °C in steps of 25 K and approximately 24 h holding time each. The mole fraction of Ar (χ_{Ar}) was used as internal standard to correct the measured concentrations of all compounds (χ_i) according to Eq. (5)

$$\chi_{\mathrm{i,corrected}} = \chi_{\mathrm{i}} \frac{\chi_{Ar\ (\mathrm{out,ref})}}{\chi_{Ar\ (\mathrm{out,\ reactor})}} \quad (5)$$

The conversion of carbon dioxide (X_{CO2}) was calculated based on the change of CO_2 concentration after passing the reactor as in Eq. (6).

$$X_{CO_2} = 1 - \frac{\chi_{CO2\ (\mathrm{out,\ reactor})}}{\chi_{CO2\ (\mathrm{out,\ ref})}} \quad (6)$$

$\chi_{CO2\ (out,\ reactor)}$ is the molar concentration of CO_2 in the outlet gas of the respective reactor and $\chi_{CO2\ (out,\ ref)}$ is the concentration of CO_2 in the outlet of the (inert) reference reactor. The selectivity for each product (S_i) was determined based on its outlet concentration and the amount of converted CO_2 according to Eq. (7).

$$S_i = \frac{\chi_{i\ (\mathrm{out,\ reactor})}}{\chi_{CO2\ (\mathrm{in,\ reactor})}}\ C_i\ X_{CO_2}^{-1} \quad (7)$$

$\chi_{i\ (out,\ reactor)}$ is the molar concentration of the respective product (e.g., MeOH) in the reactor outlet, $\chi_{CO2\ (in,\ reactor)}$ the concentration of CO_2 being dosed in the reactor and C_i is the carbon-number. The space-time yield (STY_i) was calculated from the flowrate of the respective product concentration ($\dot{\chi}_i$) in the reactor outlet and its molecular weight (MW_i) as in Eq. (8).

$$STY_i = \frac{\dot{\chi}_{i\ (out)}\ MW_i}{a_{cat}} \quad (8)$$

The quotient a_{cat} is a specific property of the catalyst on which the *STY* is fixed (e.g., its volume or mass of indium).

3 Results and Discussion

3.1 Proof of Concept

The N_2O reactive frontal chromatography (RFC) was tested for the quantification of partially reduced or undercoordinated sites on indium oxide catalysts. At first, N_2O RFC was applied on bulk indium oxide and In_2O_3 supported on monoclinic ZrO_2 (m-ZrO_2) via incipient wetness impregnation (IWI). The amount of N_2O consumed equals the amount of oxygen atoms inserted in the vacancies (O_{vac}) at the catalyst surface (Sect. 2.4).

In Fig. 2, the number of inserted oxygen atoms per square meter of sample is compared to the conversion of CO_2 and space-time yield of methanol (*STY* MeOH) at 250 °C. To rule out the differences in densities, the *STY* is depicted per volume of catalyst (mL). ZrO_2 did not consume any oxygen atoms and showed nearly no CO_2 conversion (< 0.75 %). Moreover, the selectivity of MeOH was approximately 74 % for all indium catalysts under these conditions. For the bulk indium oxide and supported indium catalysts, the conversion of CO_2 and *STY* scaled with the amount of inserted oxygen (Fig. 2a).

The typical range of oxygen vacancy abundance was 2.5 to 3.5 µmol per square meter of the measured material. The number of O_{vac} per m^2 increased by 12 % from bulk to supported indium oxide (7.9 wt % In). At the same time, the conversion and *STY* were 31 % and 35% higher, respectively. Therefore, the supported catalyst produced 35 % more methanol per hour while holding 12 % more oxygen vacancies per surface area. Increased loading (9.5 wt % In) led to 7.6 % more O_{vac} while providing 13 % higher *STY* when compared to the catalyst with 7.9 wt % In.

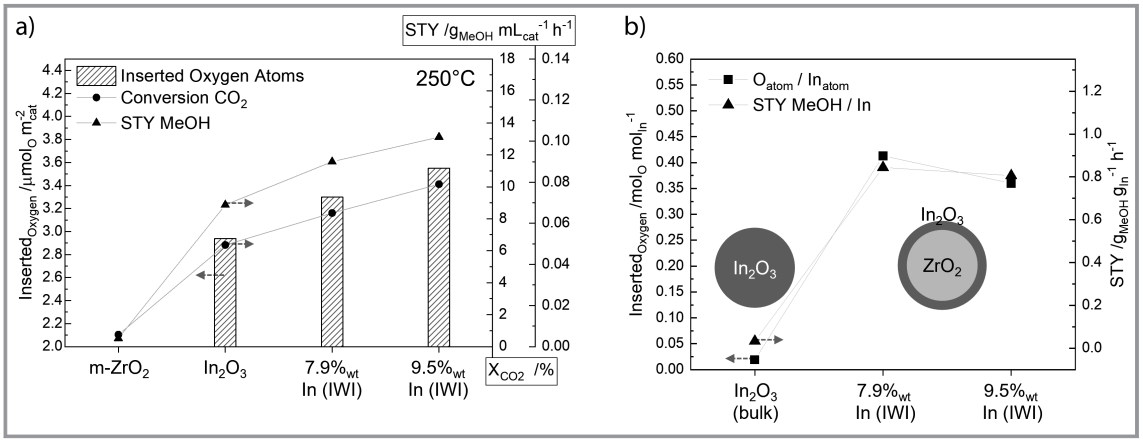

Figure 2. a) Conversion of CO_2 (X_{CO2}) and space-time yield of methanol (*STY*) plotted next to the number of inserted oxygen atoms by the N_2O RFC method. b) Indium-based *STY* and the moles of inserted oxygen atoms per moles of indium. Samples marked with IWI were prepared by incipient wetness impregnation on ZrO_2. Reaction conditions: $T = 250\,°C$, $P = 80$ bar, $H_2/CO_2 = 4{:}1$ and $GHSV = 6000\,h^{-1}$.

Moreover, both supported catalysts attracted the insertion of around 0.4 moles of O-atoms per moles of total In-atoms (Fig. 2b). This indicates that both catalysts had a similar accessibility of indium sites. The respective *STY* per gram of In was ca. 0.8 $g_{MeOH}g_{Indium}^{-1}h^{-1}$ for both. However, the bulk oxide only resulted in 0.02 O/In atoms as most of its indium is located inside the particles. The much lower O/In ratio of the bulk oxide suggests that only the surface was reduced and formed oxygen vacancies. In the following sections, ALD was applied to proof this hypothesis as it generally leads to homogeneous sub-monolayers of indium oxides.

3.2 Enhanced Dispersion of Indium by ALD

In order to further increase the dispersion and atomic efficiency of indium, ALD was applied on m-ZrO_2. One and two cycles of InO_x ALD were conducted, which led to a loading of 7.9 wt % and 14.9 wt % In, respectively. Specific characteristics of all catalysts within the study are displayed in Tab. 1.

As a result, the X-ray diffraction (XRD) pattern of all supported In_2O_3 catalysts were almost identical to that of pure m-ZrO_2 (Fig. 3a). However, the samples prepared by IWI showed an emerging reflection around 30.5° (2θ). Typically, cubic In_2O_3 exhibits a reflection of its (222) plane at a similar position, which indicates that IWI led to the formation of crystallites [61]. The catalysts synthesized by ALD did not possess additional phases suggesting an XRD-amorphous and dispersed indium oxide (InO_x).

Furthermore, STEM was conducted to elucidate the dispersion of the deposited oxides (Fig. 3b). The ALD sample (one cycle) showed evenly distributed indium along the scanned ZrO_2 particles. Moreover, the atomic ratio between In and Zr had a maximum of 1:11 and minimum of 1:13 in the energy dispersive mappings (EDX mapping). Indium was also distributed all over the particles of the IWI sample (9.5 wt % In). However, the In-signal was clearly enriched at some regions leading to a maximum In/Zr ratio of 1:4 and minimum of 1:28. Therefore, ALD resulted in a higher dispersion of indium on ZrO_2, which agrees with the XRD results. Generally, agglomeration is prevented by ALD as the deposition is limited by the number of reactive sites [41, 56].

Table 1. Characteristics of the examined catalysts.

Catalyst	Synthesis	Mass fraction of indium [%][c)]	Surface area [m^2g^{-1}][d)]	Inserted oxygen atoms [$\mu mol_O m^{-2}$][e)]	Selectivity to MeOH [%][f)]	Selectivity to CO (RWGS) [%][f)]
In_2O_3	Precipitation	82.7	46	2.94	71	28
7.9%-In_2O_3/ZrO_2	IWI[a)]	7.9	86	3.30	67	33
9.5%-In_2O_3/ZrO_2	IWI	9.5	84	3.55	67[g)]	32[g)]
(1c) InO_x/ZrO_2	ALD[b)]	7.4	79	4.36	67	33
(2c) InO_x/ZrO_2	ALD	14.9	72	3.96	67	33

a) Incipient wetness impregnation; b) atomic layer deposition; c) by ICP-OES; d) by N_2-physisorption and BET method; e) by N_2O RFC; f) at 275 °C, 80 bar, $H_2{:}CO_2 = 4{:}1$, $GHSV = 12\,000\,h^{-1}$; g) $GHSV = 6000\,h^{-1}$.

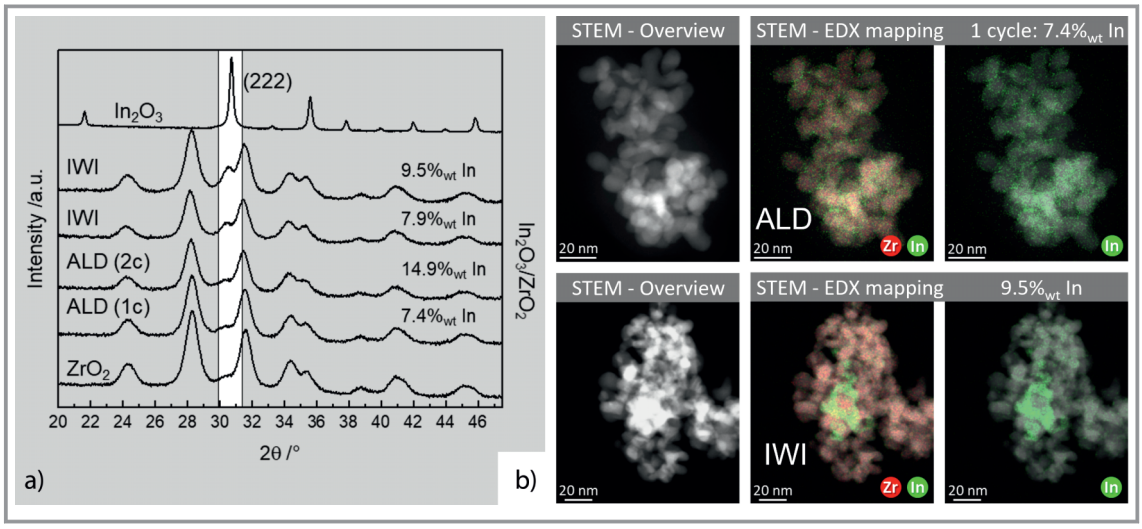

Figure 3. a) X-ray diffractograms of bulk In_2O_3 and In_2O_3 supported on monoclinic ZrO_2 by incipient wetness impregnation (IWI) or atomic layer deposition (ALD). b) STEM-HAADF images and EDX-mappings of (top) one cycle InO_x ALD on m-ZrO_2 (7.4 wt % In) and (bottom) In_2O_3 supported on m-ZrO_2 (9.5 wt % In-loading).

3.3 Activation of the Indium Oxide Catalysts

In order to titrate the oxygen vacancies, the samples had to be activated before N_2O RFC. The activation was conducted in 10 % H_2 (in N_2) at 275 °C to remain within the temperature regime of the CO_2 hydrogenation tests (Sect. 2.4). During catalytic testing, the oxide is additionally exposed to CO, contained in the syngas feed or deriving from the RWGS reaction. CO is a strong reducing agent and known to induce oxygen vacancies at the interface of Cu/ZnO or Au/CeO_2 [62, 63]. Therefore, the number of vacancies might even be higher under reaction conditions. However, at this time in situ N_2O RFC experiments were not possible. The activation with H_2 already led to a clear correlation between the N_2O consumption and the performance.

The temperature-programmed reduction (H_2-TPR) of the supported In_2O_3 showed one distinct hydrogen consumption peak at 210 °C (Fig. 4a). Moreover, the reduction of the bulk In_2O_3 occurred around 675 °C with an on-set temperature of 430 °C. Therefore, the supported In_2O_3 might only be partially reduced to indium and indium hydroxide at 275 °C. The formation of unsaturated indium indicates the existence of oxygen defects after the activation at 275 °C [17]. This agrees with the N_2O RFC results as a reductive pretreatment was necessary to convert N_2O and insert oxygen atoms. XPS of the indium region (In3d) revealed In(3+) as the major oxidation state even after the reductive treatment at 275 °C (Fig. 4b) [37]. This suggests that oxygen vacancies are exclusively formed at the outer layer.

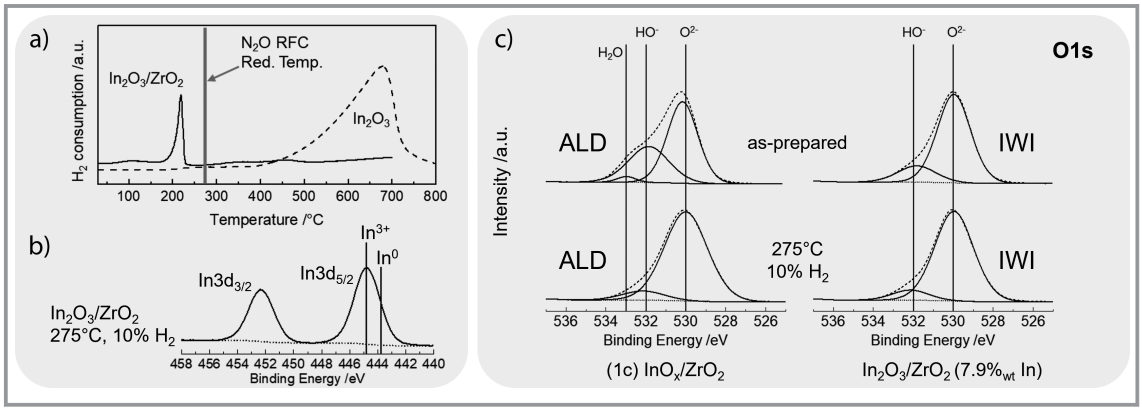

Figure 4. a) Temperature-programmed reduction (TPR) of 7.9 wt % In_2O_3/ZrO_2 (IWI) and bulk oxide (In_2O_3) under 10 vol % H_2 in N_2 until 700 or 800 °C, respectively (6 K min^{-1} rate). b) Photoemission spectrum (XPS) of the In3d region of reduced 7.9 wt % In_2O_3/ZrO_2 (IWI). c) Photoemission spectrum (XPS) of the O1s regions of (top) as-prepared and (bottom) reduced In_2O_3/ZrO_2 samples.

Furthermore, XPS of the O1s binding energy (BE) region was conducted to identify different oxygen species in the outer layer of the catalysts (up to 1 nm depth) [64]. The signal of the ALD sample (one cycle) was deconvoluted into 36 % OH-groups (BE = 532 ± 0.1 eV) and 63 % lattice oxygen (BE = 530 ± 0.1 eV, O^{2-}) (Fig. 4c) [37]. In contrast, the IWI sample (In_2O_3/ZrO_2) possessed only 17 % OH and 83 % O^{2-}. The higher abundance of OH groups on the ALD sample can be rationalized by the usage of H_2O as reagent during synthesis. Furthermore, it was shown that ALD favored the deposition of $In(OH)_x$ in the first cycles [56].

Nevertheless, XPS clearly demonstrated that both samples (ALD and IWI) exhibited the same oxygen species distribution after the activation step (Fig. 4c). Furthermore, the reductive and thermal treatment resulted in the removal of OH groups. Therefore, a similar oxide species can be assumed for both catalyst types under the applied conditions. Eventually, XPS data could not be correlated with the CO_2 hydrogenation activity as it was suggested in the literature [24, 32]. Moreover, every tested indium oxide catalyst provided the same selectivity towards MeOH and the reverse water-gas shift reaction (Tab. 1). Therefore, the presence of the same indium oxide species under reductive atmosphere is also indicated by the catalytic behavior.

3.4 CO_2 Hydrogenation Activity of the ALD Catalysts

The catalysts prepared by one and two ALD cycle (1c, 2c) of indium oxide were examined by the same N_2O RFC method. The measured number of inserted oxygen atoms was plotted against the CO_2 hydrogenation activity in Fig. 5a. Both ALD catalysts led to an increased consumption of N_2O when compared to the impregnated samples. The highest number of oxygen vacancies was found for the ALD catalyst (one cycle, 7.4 wt % In) reaching 4.36 $\mu mol_O m^{-2}$. Consequently, the 1c sample resulted in the highest conversion of CO_2 with 18.5 % at 275 °C. For instance, the typical CO_2 conversion of indium-based catalysts was reported in a range of 2–17 % at 275 °C [15, 17, 30, 32, 65]. Yet, a direct comparison would be misleading, as for every published example the conditions were different (e.g., pressure, flow rate or the addition of platin group metals).

Similar to the performance at 250 °C (Fig. 2), the conversion and *STY* scaled with the number of oxygen atoms inserted by the N_2O RFC. Moreover, the 1c ALD catalyst provided a *STY* of 0.35 $g_{MeOH} mL^{-1} h^{-1}$, which was the highest value within the study at 275 °C (= 0.24 $g_{MeOH} g^{-1} h^{-1}$). Interestingly, both ALD catalysts obtained higher activity than the impregnated sample despite the different indium loadings. This indicates that the ALD samples exhibited a similar amount of exposed and active indium sites.

The indium-based *STY* of the impregnated catalyst (IWI) was 3.0 $g_{MeOH} g_{In}^{-1} h^{-1}$, which is similar to ZrO_2-supported indium oxides in the literature [15, 17, 65]. However, the 2c ALD sample achieved a lower methanol productivity based on the mass of incorporated indium (Fig. 5b). Additionally, the number of inserted oxygens per total atoms of indium was almost 50 % lower compared to the IWI catalyst. Therefore, the ratio between the exposed indium sites and total indium was higher on the IWI sample, which might be caused by the lower loading (8 wt % vs. 14 wt % In). It was previously shown that a monolayer of In_2O_3 is formed after the second ALD cycle [56]. Hence, some indium atoms are already located in the sublayer after two ALD cycles. This supports the hypothesis, that only the exposed and unsaturated indium sites are probed by N_2O.

Finally, the highest usability or atomic efficiency of indium exhibited the 1c ALD sample with a productivity of 3.3 $g_{MeOH} g_{In}^{-1} h^{-1}$. This agrees with the number of consumed oxygen atoms and the dispersion visualized by XRD and STEM analysis (Sect. 3.2).

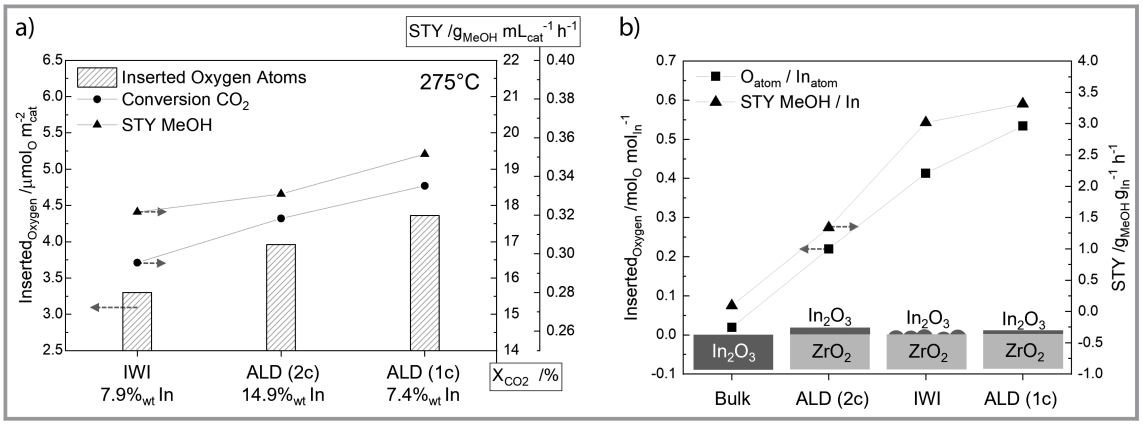

Figure 5. a) Conversion of CO_2 (X_{CO2}) and space-time yield of methanol (*STY*) plotted next to the number of inserted oxygen atoms by the N_2O RFC method. b) Indium-based *STY* and the moles of inserted oxygen atoms per moles of indium. Samples marked with IWI were prepared by incipient wetness impregnation on ZrO_2. 1c and 2c indicate the number of InO_x ALD cycles conducted on ZrO_2. Reaction conditions: T = 275 °C, P = 80 bar, H_2/CO_2 = 4:1 and $GHSV$ = 12 000 h^{-1}.

3.5 Number of Exposed Indium Atoms at the Surface

As shown above, N_2O RFC can quantitatively probe oxygen vacancies on the partially reduced indium oxide surface. Thereby, the number of consumed oxygen atoms is in stoichiometric ratio to the number of indium atoms of the sample. Interestingly, the highest number of oxygen atoms consumed per incorporated indium atom was approximately 0.5 O/In (Fig. 5b). Typically, the N_2O RFC on copper surfaces is reported to also insert one oxygen atom per two copper atoms [57, 58]. Especially, the 1c ALD sample exhibited a ratio of 0.53 O/In while the agglomeration of indium was ruled out by XRD and STEM.

Hence, it is likely that two indium atoms, exposed at the surface and undercoordinated by oxygen, indeed adsorb one oxygen atom (after the reduction at 10 % H_2 at 275 °C). Eventually, the number of exposed indium atoms could be calculated from the number of consumed oxygen atoms, considering the respective surface area and a ratio of 0.5 O/In for all catalysts (Fig. 6).

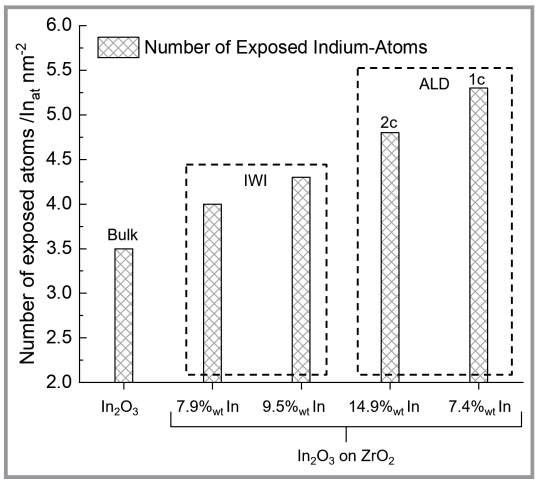

Figure 6. The number of exposed indium atoms per square nanometer of surface area estimated from N_2O RFC results. The denotation IWI indicates incipient wetness impregnation and 1c/2c is the number of ALD cycles.

For example, the 1c ALD sample exhibited 5.3 indium atoms per nm^2 which formed exposed oxygen vacancies. In order to evaluate this finding, the maximum possible number of surface indium atoms (on ZrO_2) was calculated based on the loading (7.4 wt % In) and surface area. As a result, the maximum number of exposed indium atoms was 4.9 nm^{-2} considering a homogeneous distribution. Therefore, the value determined by the N_2O RFC is similar to the one found by the approximation. Additionally, the outer layer of the (111) facet of cubic In_2O_3 also typically holds 5–6 Indium atoms per nm^2 [66, 67]. However, the number of exposed indium atoms was determined 3.5–4.3 nm^{-2} for the bulk oxide and samples prepared by IWI (Fig. 6). This indicates that the RFC method exclusively titrates accessible oxygen vacancies with N_2O. Eventually, the ALD catalysts exhibited a higher number of exposed vacancies which agrees with the superior CO_2 hydrogenation activity.

4 Conclusion

For the first time, N_2O reactive frontal chromatography was used to titrate the surface of partially reduced indium oxides. Thereby, N_2O was shown to quantitatively fill the oxygen vacancies at undercoordinated indium sites. The RFC method was applied on bulk oxide and ZrO_2-supported In_2O_3 prepared by incipient wetness impregnation. As a result, the respective CO_2 hydrogenation activity correlated with the number of inserted oxygen atoms on the catalysts. Consequently, the formation rate of methanol scaled with the number of oxygen vacancies per surface area. The supported In_2O_3 had an increased utilization of indium as the space-time yield per mass of indium was over ten times higher than for the bulk oxide. Furthermore, the number of oxygen vacancies per moles of indium was also determined to be ten times higher in the case of the supported In_2O_3.

Moreover, atomic layer deposition of indium oxide was applied on ZrO_2 to further improve the indium utilization. The superior dispersion of the ALD catalysts compared to the samples prepared by IWI was indicated by XRD and STEM-EDX mappings. Eventually, the enhanced distribution of indium was confirmed by N_2O RFC as the ALD catalyst exhibited up to 30 % more oxygen vacancies on the surface. After a reductive treatment in hydrogen at 275 °C, the oxidic species on the ALD catalysts was found to be similar to the IWI samples by XPS analysis. Therefore, both catalyst designs are suggested to have the same surface termination under reaction conditions. This was also indicated by the catalytical performance as the product selectivity was the same for the ALD and IWI samples.

The CO_2 conversion as well as the formation rate of methanol was higher for the ALD samples which is in line with the number of oxygen vacancies per surface area. Especially the catalyst with one ALD cycle possessed a superior rate of methanol formation per mass of indium and highest oxygen insertion per mole of indium. Therefore, ALD was successfully applied to further enhance the indium utilization and atomic efficiency compared to IWI. Finally, the number of exposed indium atoms of the catalysts could be determined by the N_2O RFC method. The resulting number of surface indium atoms might be utilized as an indicator for the dispersion of indium oxide in future studies.

Supporting Information

Supporting Information for this article can be found under DOI: https://doi.org/10.1002/cite.202200085.

The authors gratefully acknowledge financial support from the Deutsche Forschungsgemeinschaft (DFG, German Research Foundation) under Germany's Excellence Strategy–EXC 2008–390540038–UniSysCat. The authors want to thank the following colleagues: Kevin Profita, Sophie Hund (TU Berlin), Maike Hashagen and Christian Rohner (FHI). The work was conducted in the framework of the BasCat JointLab between BASF SE, the TU Berlin, and the FHI. We also thank the Berlin Cluster of Excellence UniSysCat for the support. Open access funding enabled and organized by Projekt DEAL.

Symbols used

$\Delta G^0_{298.15K}$	[kJ mol^{-1}]	Gibbs free energy of the reaction at 298.15 K
GHSV	[h^{-1}]	gas-hourly space velocity
Inserted$_{Oxygen}$	[μmol$_O$m^{-2}; mol$_O$mol$_{In}^{-1}$]	moles of inserted oxygen per surface area or per moles of indium
MW	[g mol^{-1}]	molecular weight
STY	[$g_{MeOH}mL_{cat}^{-1}h^{-1}$; $g_{MeOH}g_{In}^{-1}h^{-1}$]	space-time yield of methanol per catalyst volume or per mass of indium
X	[%]	conversion of CO_2
χ_i	[mol s^{-1}]	molar concentration flow
θ	[°]	scattering angle in XRD

Sub- and Superscripts

at	atoms
cat	catalyst
In	indium atoms
O	oxygen atoms
vac	vacancies

Abbreviations

1c	one ALD cycle
ALD	atomic layer deposition
BET	Brunauer-Emmett-Teller method
EDX	energy dispersive X-Ray analysis
HAADF	high-angle annular dark-field imaging
ICP-OES	inductively coupled plasma atomic emission spectroscopy
IWI	incipient wetness impregnation
MeOH	methanol
MS	mass spectrometer/ spectroscopy
m-ZrO_2	monoclinic zirconia
O_{vac}	oxygen vacancy
RFC	reactive frontal chromatography
RWGS	reverse water-gas shift
STEM	scanning transmission electron microscopy
XPS	X-ray photoelectron spectroscopy
XRD	(powder) X-ray diffraction

References

[1] M. Bowker, *ChemCatChem* **2019**, *11 (17)*, 4238–4246. DOI: https://doi.org/10.1002/cctc.201900401
[2] J. Ma, N. Sun, X. Zhang, N. Zhao, F. Xiao, W. Wei, Y. Sun, *Catal. Today* **2009**, *148 (3–4)*, 221–231. DOI: https://doi.org/10.1016/j.cattod.2009.08.015
[3] E. Schwab, A. Milanov, S. A. Schunk, A. Behrens, N. Schödel, *Chem. Ing. Tech.* **2015**, *87 (4)*, 347–353. DOI: https://doi.org/10.1002/cite.201400111
[4] M. J. Bos, S. Kersten, D. Brilman, *Appl. Energy* **2020**, *264*, 114672. DOI: https://doi.org/10.1016/j.apenergy.2020.114672
[5] www.methanol.org/methanol-price-supply-demand/ (Accessed on May 05, 2022)
[6] M. S. Alias, S. K. Kamarudin, A. M. Zainoodin, M. S. Masdar, *Int. J. Hydrogen Energy* **2020**, *45 (38)*, 19620–19641. DOI: https://doi.org/10.1016/j.ijhydene.2020.04.202
[7] S. Verhelst, J. W. G. Turner, L. Sileghem, J. Vancoillie, *Prog. Energy Combust. Sci.* **2019**, *70*, 43–88. DOI: https://doi.org/10.1016/j.pecs.2018.10.001
[8] M. Behrens, F. Studt, I. Kasatkin, S. Kühl, M. Hävecker, F. Abild-Pedersen, S. Zander, F. Girgsdies, P. Kurr, B.-L. Kniep, M. Tovar, R. W. Fischer, J. K. Nørskov, R. Schlögl, *Science* **2012**, *336 (6083)*, 893–897. DOI: https://doi.org/10.1126/science.1219831
[9] M. González-Castaño, B. Dorneanu, H. Arellano-García, *React. Chem. Eng.* **2021**, *6 (6)*, 954–976. DOI: https://doi.org/10.1039/D0RE00478B
[10] C. Álvarez Galván, J. Schumann, M. Behrens, J. L. G. Fierro, R. Schlögl, E. Frei, *Appl. Catal., B* **2016**, *195*, 104–111. DOI: https://doi.org/10.1016/j.apcatb.2016.05.007
[11] O.-S. Joo, K.-D. Jung, I. Moon, A. Y. Rozovskii, G. I. Lin, S.-H. Han, S.-J. Uhm, *Ind. Eng. Chem. Res.* **1999**, *38 (5)*, 1808–1812. DOI: https://doi.org/10.1021/ie9806848
[12] T. Lunkenbein, F. Girgsdies, T. Kandemir, N. Thomas, M. Behrens, R. Schlögl, E. Frei, *Angew. Chem., Int. Ed.* **2016**, *55 (41)*, 12708–12712. DOI: https://doi.org/10.1002/anie.201603368
[13] M. B. Fichtl, D. Schlereth, N. Jacobsen, I. Kasatkin, J. Schumann, M. Behrens, R. Schlögl, O. Hinrichsen, *Appl. Catal., A* **2015**, *502*, 262–270. DOI: https://doi.org/10.1016/j.apcata.2015.06.014
[14] B. Liang, J. Ma, X. Su, C. Yang, H. Duan, H. Zhou, S. Deng, L. Li, Y. Huang, *Ind. Eng. Chem. Res.* **2019**, *58 (21)*, 9030–9037. DOI: https://doi.org/10.1021/acs.iecr.9b01546
[15] J. Wang, G. Zhang, J. Zhu, X. Zhang, F. Ding, A. Zhang, X. Guo, C. Song, *ACS Catal.* **2021**, *11 (3)*, 1406–1423. DOI: https://doi.org/10.1021/acscatal.0c03665
[16] K. Sun, Z. Fan, J. Ye, J. Yan, Q. Ge, Y. Li, W. He, W. Yang, C. Liu, *J. CO2 Util.* **2015**, *12*, 1–6. DOI: https://doi.org/10.1016/j.jcou.2015.09.002
[17] O. Martin, A. J. Martín, C. Mondelli, S. Mitchell, T. F. Segawa, R. Hauert, C. Drouilly, D. Curulla-Ferré, J. Pérez-Ramírez, *Angew. Chem., Int. Ed.* **2016**, *55 (21)*, 6261–6265. DOI: https://doi.org/10.1002/anie.201600943
[18] O. Martin, C. Mondelli, D. Curulla-Ferré, C. Drouilly, R. Hauert, J. Pérez-Ramírez, *ACS Catal.* **2015**, *5 (9)*, 5607–5616. DOI: https://doi.org/10.1021/acscatal.5b00877
[19] J. Ye, C. Liu, D. Mei, Q. Ge, *ACS Catal.* **2013**, *3 (6)*, 1296–1306. DOI: https://doi.org/10.1021/cs400132a
[20] M. S. Frei, M. Capdevila-Cortada, R. García-Muelas, C. Mondelli, N. López, J. A. Stewart, D. Curulla Ferré, J. Pérez-Ramírez, *J. Catal.* **2018**, *361*, 313–321. DOI: https://doi.org/10.1016/j.jcat.2018.03.014

[21] M. S. Frei, C. Mondelli, A. Cesarini, F. Krumeich, R. Hauert, J. A. Stewart, D. Curulla Ferré, J. Pérez-Ramírez, *ACS Catal.* **2020**, *10 (2)*, 1133–1145. DOI: https://doi.org/10.1021/acscatal.9b03305

[22] P. Gao, S. Dang, S. Li, X. Bu, Z. Liu, M. Qiu, C. Yang, H. Wang, L. Zhong, Y. Han, Q. Liu, W. Wei, Y. Sun, *ACS Catal.* **2018**, *8 (1)*, 571–578. DOI: https://doi.org/10.1021/acscatal.7b02649

[23] C. Y. Regalado Vera, N. Manavi, Z. Zhou, L.-C. Wang, W. Diao, S. Karakalos, B. Liu, K. J. Stowers, M. Zhou, H. Luo, D. Ding, *Chem. Eng. J.* **2021**, *426*, 131767. DOI: https://doi.org/10.1016/j.cej.2021.131767

[24] S. Dang, P. Gao, Z. Liu, X. Chen, C. Yang, H. Wang, L. Zhong, S. Li, Y. Sun, *J. Catal.* **2018**, *364*, 382–393. DOI: https://doi.org/10.1016/j.jcat.2018.06.010

[25] J. Ye, C. Liu, D. Mei, Q. Ge, *ACS Catal.* **2013**, *3 (6)*, 1296–1306. DOI: https://doi.org/10.1021/cs400132a

[26] J. Ye, C. Liu, Q. Ge, *J. Phys. Chem. C* **2012**, *116 (14)*, 7817–7825. DOI: https://doi.org/10.1021/jp3004773

[27] A. Cao, Z. Wang, H. Li, J. K. Nørskov, *ACS Catal.* **2021**, *11 (3)*, 1780–1786. DOI: https://doi.org/10.1021/acscatal.0c05046

[28] B. Qin, S. Li, *Phys. Chem. Chem. Phys.* **2020**, *22 (6)*, 3390–3399. DOI: https://doi.org/10.1039/c9cp05867b

[29] A. Posada-Borbón, H. Grönbeck, *Phys. Chem. Chem. Phys.* **2019**, *21 (39)*, 21698–21708. DOI: https://doi.org/10.1039/c9cp04097h

[30] M. S. Frei, C. Mondelli, R. García-Muelas, K. S. Kley, B. Puértolas, N. López, O. V. Safonova, J. A. Stewart, D. Curulla Ferré, J. Pérez-Ramírez, *Nat. Commun.* **2019**, *10 (1)*, 3377. DOI: https://doi.org/10.1038/s41467-019-11349-9

[31] K. Sun, N. Rui, Z. Zhang, Z. Sun, Q. Ge, C. Liu, *Green Chem.* **2020**, *22 (15)*, 5059–5066. DOI: https://doi.org/10.1039/D0GC01597K

[32] N. Rui, Z. Wang, K. Sun, J. Ye, Q. Ge, C. Liu, *Appl. Catal., B* **2017**, *218*, 488–497. DOI: https://doi.org/10.1016/j.apcatb.2017.06.069

[33] M. Dou, M. Zhang, Y. Chen, Y. Yu, *Comput. Theor. Chem.* **2018**, *1126*, 7–15. DOI: https://doi.org/10.1016/j.comptc.2018.01.008

[34] S. Peng, F. Gong, L. Li, D. Yu, D. Ji, T. Zhang, Z. Hu, Z. Zhang, S. Chou, Y. Du, S. Ramakrishna, *J. Am. Chem. Soc.* **2018**, *140 (42)*, 13644–13653. DOI: https://doi.org/10.1021/jacs.8b05134

[35] F. Lei, Y. Sun, K. Liu, S. Gao, L. Liang, B. Pan, Y. Xie, *J. Am. Chem. Soc.* **2014**, *136 (19)*, 6826–6829. DOI: https://doi.org/10.1021/ja501866r

[36] H. Idriss, *Surf. Sci.* **2021**, *712*, 121894. DOI: https://doi.org/10.1016/j.susc.2021.121894

[37] Z. M. Detweiler, S. M. Wulfsberg, M. G. Frith, A. B. Bocarsly, S. L. Bernasek, *Surf. Sci.* **2016**, *648*, 188–195. DOI: https://doi.org/10.1016/j.susc.2015.10.026

[38] M. Wajid Shah, Y. Zhu, X. Fan, J. Zhao, Y. Li, S. Asim, C. Wang, *Sci. Rep.* **2015**, *5*, 15804. DOI: https://doi.org/10.1038/srep15804

[39] H. Yuan, J. Li, W. Yang, Z. Zhuang, Y. Zhao, L. He, L. Xu, X. Liao, R. Zhu, L. Mai, *ACS Appl. Mater. Interfaces* **2018**, *10 (19)*, 16410–16417. DOI: https://doi.org/10.1021/acsami.8b01209

[40] J. Strunk, K. Kähler, X. Xia, M. Comotti, F. Schüth, T. Reinecke, M. Muhler, *Appl. Catal., A* **2009**, *359 (1–2)*, 121–128. DOI: https://doi.org/10.1016/j.apcata.2009.02.030

[41] R. L. Puurunen, *J. Appl. Phys.* **2005**, *97 (12)*, 121301. DOI: https://doi.org/10.1063/1.1940727

[42] G. Dingemans, R. Seguin, P. Engelhart, M. C. M. de van Sanden, W. M. M. Kessels, *Phys. Status Solidi RRL* **2010**, *4 (1-2)*, 10–12. DOI: https://doi.org/10.1002/pssr.200903334

[43] H.-M. Cheng, F.-M. Wang, J. P. Chu, R. Santhanam, J. Rick, S.-C. Lo, *J. Phys. Chem. C* **2012**, *116 (14)*, 7629–7637. DOI: https://doi.org/10.1021/jp210551r

[44] C. A. Wilson, R. K. Grubbs, S. M. George, *Chem. Mater.* **2005**, *17 (23)*, 5625–5634. DOI: https://doi.org/10.1021/cm050704d

[45] B. J. O'Neill, D. H. K. Jackson, J. Lee, C. Canlas, P. C. Stair, C. L. Marshall, J. W. Elam, T. F. Kuech, J. A. Dumesic, G. W. Huber, *ACS Catal.* **2015**, *5 (3)*, 1804–1825. DOI: https://doi.org/10.1021/cs501862h

[46] *Nanotechnology in Catalysis* (Eds: M. van de Voorde, B. Sels), Wiley-VCH, Weinheim **2017**. DOI: https://doi.org/10.1002/9783527699827

[47] A. J. M. Mackus, M. J. Weber, N. F. W. Thissen, D. Garcia-Alonso, R. H. J. Vervuurt, S. Assali, A. A. Bol, M. A. Verheijen, W. M. M. Kessels, *Nanotechnol.* **2016**, *27 (3)*, 34001. DOI: https://doi.org/10.1088/0957-4484/27/3/034001

[48] W.-J. Lee, S. Bera, H.-C. Shin, W.-P. Hong, S.-J. Oh, Z. Wan, S.-H. Kwon, *Adv. Mater. Interfaces* **2019**, *6 (21)*, 1970133. DOI: https://doi.org/10.1002/admi.201970133

[49] L. Geerts, R. K. Ramachandran, J. Dendooven, S. Radhakrishnan, J. W. Seo, C. Detavernier, J. Martens, S. P. Sree, *Catal. Sci. Technol.* **2020**, *10 (6)*, 1778–1788. DOI: https://doi.org/10.1039/C9CY02610J

[50] H. Yan, K. He, I. A. Samek, D. Jing, M. G. Nanda, P. C. Stair, J. M. Notestein, *Science* **2021**, *371 (6535)*, 1257–1260. DOI: https://doi.org/10.1126/science.abd4441

[51] N. Yan, L. Qin, J. Li, F. Zhao, H. Feng, *Appl. Surf. Sci.* **2018**, *451*, 155–161. DOI: https://doi.org/10.1016/j.apsusc.2018.04.247

[52] P. Ingale, C. Guan, R. Kraehnert, R. Naumann d'Alnoncourt, A. Thomas, F. Rosowski, *Catal. Today* **2021**, *362*, 47–54. DOI: https://doi.org/10.1016/j.cattod.2020.04.050

[53] P. Ingale, K. Knemeyer, P. Preikschas, M. Ye, M. Geske, R. Naumann d'Alnoncourt, A. Thomas, F. Rosowski, *Catal. Sci. Technol.* **2021**, *11 (2)*, 484–493. DOI: https://doi.org/10.1039/D0CY01528H

[54] J. Gao, P. E. Boahene, Y. Hu, A. Dalai, H. Wang, *Catalysts* **2019**, *9 (11)*, 922. DOI: https://doi.org/10.3390/catal9110922

[55] V. E. Strempel, R. Naumann d'Alnoncourt, M. Driess, F. Rosowski, *Rev. Sci. Instrum.* **2017**, *88 (7)*, 74102. DOI: https://doi.org/10.1063/1.4992023

[56] R. Baumgarten, P. Ingale, K. Knemeyer, R. Naumann d'Alnoncourt, M. Driess, F. Rosowski, *Nanomater.* **2022**, *12 (9)*, 1458. DOI: https://doi.org/10.3390/nano12091458

[57] G. Chinchen, *J. Catal.* **1987**, *103 (1)*, 79–86. DOI: https://doi.org/10.1016/0021-9517(87)90094-7

[58] O. Hinrichsen, T. Genger, M. Muhler, *Chem. Eng. Technol.* **2000**, *23 (11)*, 956–959. DOI: https://doi.org/10.1002/1521-4125(200011)23:11<956:AID-CEAT956>3.0.CO;2-L

[59] S. Tada, M. Yokoyama, R. Kikuchi, T. Haneda, H. Kameyama, *J. Phys. Chem. C* **2013**, *117 (28)*, 14652–14658. DOI: https://doi.org/10.1021/jp404291k

[60] R. Naumann d'Alnoncourt, B. Graf, X. Xia, M. Muhler, *J. Therm. Anal. Calorim.* **2008**, *91 (1)*, 173–179. DOI: https://doi.org/10.1007/s10973-007-8446-4

[61] S. Tan, L. B. Gil, N. Subramanian, D. S. Sholl, S. Nair, C. W. Jones, J. S. Moore, Y. Liu, R. S. Dixit, J. G. Pendergast, *Appl. Catal., A* **2015**, *498*, 167–175. DOI: https://doi.org/10.1016/j.apcata.2015.03.020

[62] R. Naumann d'Alnoncourt, X. Xia, J. Strunk, E. Löffler, O. Hinrichsen, M. Muhler, *Phys. Chem. Chem. Phys.* **2006**, *8 (13)*, 1525–1538. DOI: https://doi.org/10.1039/b515487a

[63] D. Widmann, R. Leppelt, R. Behm, *J. Catal.* **2007**, *251 (2)*, 437–442. DOI: https://doi.org/10.1016/j.jcat.2007.07.026

[64] S. Tougaard, *J. Electron Spectrosc. Relat. Phenom.* **2010**, *178–179*, 128–153. DOI: https://doi.org/10.1016/j.elspec.2009.08.005

[65] T. Chen, C. Cao, T. Chen, X. Ding, H. Huang, L. Shen, X. Cao, M. Zhu, J. Xu, J. Gao, Y.-F. Han, *ACS Catal.* **2019**, *9 (9)*, 8785–8797. DOI: https://doi.org/10.1021/acscatal.9b01869

[66] S. Z. Karazhanov, P. Ravindran, P. Vajeeston, A. Ulyashin, T. G. Finstad, H. Fjellvåg, *Phys. Rev. B* **2007**, *76 (7)*. DOI: https://doi.org/10.1103/PhysRevB.76.075129

[67] A. Walsh, C. R. A. Catlow, *J. Mater. Chem.* **2010**, *20 (46)*, 10438. DOI: https://doi.org/10.1039/c0jm01816c

